

Single-molecule FRET reveals the energy landscape of the full-length SAM-I riboswitch

Christoph Manz,^{1,2} Andrei Yu. Kobitski,¹ Ayan Samanta,³ Bettina G. Keller⁴, Andres Jäschke,^{2,3} and G. Ulrich Nienhaus^{1,2,5,6,*}.

¹ Institute of Applied Physics, Karlsruhe Institute of Technology, Wolfgang-Gaede-Str. 1, 76131 Karlsruhe, Germany

² HEiKA – Heidelberg Karlsruhe Research Partnership, Karlsruhe Institute of Technology, Hermann-von-Helmholtz Platz 1, 76344 Eggenstein-Leopoldshafen, Germany

³ Institute of Pharmacy and Molecular Biotechnology, Heidelberg University, Im Neuenheimer Feld 364, 69120 Heidelberg, Germany

⁴ Freie Universität Berlin, Institute of Chemistry and Biochemistry, Takustr. 3, 14195 Berlin, Germany

⁵ Institute of Nanotechnology and Institute of Toxicology and Genetics, Karlsruhe Institute of Technology, Hermann-von-Helmholtz-Platz 1, 76344 Eggenstein-Leopoldshafen, Germany

⁶ Department of Physics, University of Illinois at Urbana-Champaign, Urbana, Illinois 61801, USA

*Corresponding author e-mail: uli@uiuc.edu

Abstract

S-adenosyl-L-methionine (SAM) ligand binding induces major structural changes in SAM-I riboswitches, through which they regulate gene expression via transcription termination. As yet, only little is known about the conformations and motions governing the function of the full-length SAM-I riboswitch. Therefore, we have explored its conformational energy landscape as a function of Mg^{2+} and SAM ligand concentrations by using single-molecule Förster resonance energy transfer (smFRET) microscopy and hidden Markov modeling analysis. We resolved four conformational states both in the presence and absence of SAM and determined their Mg^{2+} -dependent fractional populations and conformational dynamics, including state lifetimes, interconversion rate coefficients and equilibration timescales. Riboswitches with terminator and anti-terminator folds coexist; SAM binding only gradually shifts the populations toward terminator states. We observed a pronounced acceleration of conformational transitions upon SAM binding, which may be crucial for off-switching during the brief decision window prior to expression of the downstream gene.

Riboswitches comprise a diverse group of highly structured, non-coding RNA elements involved in gene regulation on the transcriptional or translational level. Mostly located in the 5' untranslated region of the messenger RNA, they regulate expression of downstream genes through specific binding of metabolites, which induces major changes of the riboswitch structure¹⁻⁴. Riboswitches are ubiquitous in nature and control numerous fundamental biochemical processes; therefore, they bear great promise for a variety of applications in synthetic biology and genetic engineering, and also as possible targets for the development of antibiotics^{3,5,6}.

S-adenosyl-L-methionine (SAM) binding riboswitches are a family of transcriptional riboswitches regulating the expression of genes involved in the biosynthesis of cysteine, methionine and SAM metabolites^{7,8}. They contain two distinct functional domains, the aptamer domain and the expression platform, which compete for parts of the joining sequence. The aptamer is a biosensor capable of capturing the target metabolite in a ligand binding pocket with high specificity and selectivity. In the simplest mechanistic model, the expression platform toggles between two distinct, mutually exclusive secondary structures, depending on the ligand binding status: in the absence of metabolite, it assumes an anti-terminator (AT) stem-loop structure, leading to transcriptional read-through (ON state). Upon ligand binding, it folds into a rho-independent terminator (T) stem-loop, resulting in premature transcription termination (OFF state)^{2,6,9}. Such a description in terms of a two-state thermodynamic model appears simplistic, however, considering that complex RNA molecules typically exist in multiple conformations in equilibrium, arranged as minima in a hierarchical free energy landscape^{10,11}. In addition, the kinetics of riboswitch folding may play a decisive role in their function, considering that transcriptional riboswitches act right after or even during their synthesis but before the start of gene transcription by the RNA polymerase. Indeed, studies on other riboswitches have reported that some exert functional control via kinetic changes¹²⁻¹⁴ and others through shifts of populations in thermodynamic equilibrium^{15,16}.

Here we focus on the SAM-I riboswitch. Crystal structures of its aptamer domain with and without ligand have been solved^{1,17}, and aptamer-ligand interactions have been investigated in great

detail^{2,8,18-24}. The folded aptamer consists of four helices (P1–P4, **Fig. 1**) conjoined by a four-way junction. In the SAM-bound form, helices P1/P4 and P2/P3 are stacked coaxially together with their joining regions; a kink-turn (KT) in helix P2 and a pseudoknot (PK) motif involving P2 and the P3/P4 joining region are typical features of the compact tertiary fold that sequesters the SAM ligand in a pocket formed by helices P1 and P3 and the P1/P2 joining region^{1,24}. Unlike helices P2–P4, which are consecutive hairpin structures, helix P1 forms by long range pairing of nonadjacent strand segments from either end of the aptamer sequence. Its stabilization by the bound ligand appears essential for the switching function of the SAM riboswitch and other P1 helix-regulated riboswitches²⁵. As yet, however, experimental studies addressing the allosteric communication between the aptamer domain and the expression platform of full-length riboswitches have remained scarce^{15,16,26-28}.

We have explored the conformational energy landscape of the complete SAM-I riboswitch (169 nt, *Bacillus subtilis yitJ*) and its dependence on the Mg²⁺ ion and SAM ligand concentration by measuring single-molecule Förster resonance energy transfer (smFRET) on specifically FRET-labeled variants (**Fig. 1**). By using sophisticated data analysis tools, we have identified four key conformations for both ligand-free and ligand-bound SAM-I, determined their relative free energies and the dynamics of conformational change. T and AT riboswitch conformations (**Fig. 1c,d**) coexist in significant proportions with and without bound ligand. SAM binding causes only a moderate shift of the thermodynamic equilibrium toward T but markedly accelerates conformational dynamics, which could be essential for SAM-I riboswitch function during transcription.

Results

Mg²⁺ and SAM dependent conformational changes

We synthesized the SAM-I riboswitch from five RNA oligomers by splinted ligation²⁹. FRET pairs of dyes were introduced at suitably chosen locations so that structural changes result in sizeable FRET changes. Based on prior knowledge of the secondary and tertiary structures^{17,24}, we selected positions U₈₁ or U₁₅₀ for the donor (Cy3) dye, and U₈ for the acceptor (Cy5) dye (**Fig. 1**). Construct RS_{EA} has the donor located on the expression platform (U₁₅₀) and the acceptor on the P1 helix of the aptamer domain (U₈), and thus senses conformational changes of the expression platform with respect to the aptamer domain. Construct RS_{AA} has both dyes on the aptamer domain, the donor on P3 (U₈₁) and the acceptor again on P1 (U₈) and thus monitors aptamer reconfiguration.

Mg²⁺ ion binding is known to induce a structural collapse of the aptamer domain^{19,20,26}. To address Mg²⁺ ion effects on the conformation of the complete riboswitch, we measured the fluorescence emission from individual SAM-I molecules in two (donor/acceptor) color channels over a wide range of Mg²⁺ ion concentrations (0 – 100mM), and we also studied the effect of SAM ligand binding. From the donor and acceptor emission intensities of thousands of individual molecules, we calculated the FRET efficiency, E , and compiled FRET histograms, depicting the number of molecules within a specific FRET efficiency interval versus the FRET efficiency (**Fig. 2a–c** for selected Mg²⁺ and SAM concentrations, **Supplementary Results, Supplementary Figs. 1 and 2** for the complete data sets; the total number of analyzed molecules is given in **Supplementary Table 1**). Standard FRET histogram analysis involves fitting model distributions, usually Gaussians, centered on different mean FRET efficiency values, $\langle E \rangle$. These distributions represent conformations with different mean inter-dye distances, R , which are related to the FRET efficiency by the relation $E = R_0^6 / (R_0^6 + R^6)$. Here, R_0 is the characteristic Förster radius of the FRET dye pair (53 Å for Cy3-Cy5 used here). This analysis, however, succeeds only for a small (typically 2–3) number of well separated FRET distributions because those distributions are fairly broad due to technical issues inherent in single molecule

detection such as photon statistics and dye blinking³⁰. Moreover, structural heterogeneity within each distribution may lead to additional broadening. Oftentimes, overlapping FRET distributions can be disentangled by systematic parameter variation, e.g., Mg^{2+} ion concentration or temperature, and global fitting of many histograms with a thermodynamic model describing those variations³¹⁻³³. In this study, however, unambiguous decomposition of the broad and featureless FRET histograms was only feasible by incorporating information from a hidden Markov model (HMM) analysis of kinetic data (see below).

We can gain important insights already from a coarse interpretation of the FRET histograms. In the absence of Mg^{2+} ions, construct RS_{AA} , with donor and acceptor dyes on the aptamer domain, displays two FRET populations (**Fig. 2a**): a low-FRET minority population with $\langle E \rangle \approx 0.1$ and a majority population centered on $\langle E \rangle \approx 0.3$, which shifts markedly toward higher FRET efficiency with increasing Mg^{2+} concentration. This behavior indicates a significant decrease of the donor-acceptor distance in response to Mg^{2+} binding and thus compaction of the aptamer domain (**Fig. 2d**). The mean FRET efficiency, $\langle E \rangle \approx 0.6$ at 100 mM Mg^{2+} (**Supplementary Fig. 2**) corresponds to an inter-dye distance of ~ 49 Å. A similar Mg^{2+} induced compaction was also observed in a recent smFRET study of the *Bacillus subtilis metI* SAM-I aptamer domain (without expression platform)²⁰. There are, however, clear differences to our FRET histogram data, implying that the presence of the expression platform affects the aptamer structure. In the full-length riboswitch, there is a population below $E = 0.2$ (inter-dye distance > 67 Å) even at high Mg^{2+} concentration (**Fig. 2a**). This low-FRET population appears because Mg^{2+} induced compaction of the aptamer domain is accompanied by a population shift from T to AT conformations (**Fig. 1c,d**)^{26,34}. This change involves partial or even complete disruption of helix P1 due to strand invasion by the AT hairpin, giving rise to a low-FRET species at high Mg^{2+} concentration because the acceptor residing on U_8 in our RS_{AA} construct gets displaced from the compact aptamer moiety (**Fig. 1**).

FRET histograms of the RS_{EA} construct, which carries the donor on the expression platform and the acceptor on the aptamer domain, are shown in **Fig. 2b**. At low Mg²⁺, where the riboswitch assumes the T conformation²⁶, there is predominantly low-FRET population, with $\langle E \rangle \approx 0.2$ corresponding to an inter-dye distance of $\sim 67 \text{ \AA}$. Accordingly, the expression platform hairpin is displaced from the P1 helix due to the flexible RNA strand linking the two (**Fig. 2e**). With increasing Mg²⁺ concentration, an additional high-FRET subpopulation ($E > 0.6$) appears, showing that the expression platform moiety associates closely with the aptamer. This compact tertiary structure has been assigned to an AT conformation, in which the AT hairpin is stacked onto a partially formed P1 helix (**Fig. 2e**)²⁷.

We further measured FRET histograms of the RS_{EA} construct as a function of SAM ligand concentration in the range of 0–10 μM , keeping the Mg²⁺ concentration at 20mM to ensure a significant fraction of high-FRET molecules (**Fig. 2c and Supplementary Fig. 1**). With increasing ligand concentration, the high-FRET population ($E > 0.6$) decreases markedly. This result further supports the assignment of the high-FRET population to AT conformations (**Fig. 2b,e**) because SAM binding is expected to stabilize T conformations², featuring greater inter-dye distances due to T hairpin formation (**Fig. 2f**).

Conformational dynamics of the SAM-I riboswitch

To resolve the broad FRET histograms into separate states and to determine the kinetics of state interconversion, we measured the fluorescence emission from individual immobilized riboswitch molecules as a function of time and applied hidden Markov model (HMM) analysis to the smFRET data. Unlike FRET efficiency histogram analysis, which solely relies on spectroscopic information, HMM employs both spectroscopic and temporal information by assuming stochastic switching between a set of discrete states with well-defined average FRET efficiencies and state lifetimes³⁵⁻³⁸. HMM greatly helps to identify separate states in inevitably noisy intensity time traces and, by using

transition matrix analysis, also provides rate coefficients of conformational transitions on timescales from sub-milliseconds to seconds³⁸.

For kinetic experiments on the RS_{EA} variant, we chose buffer conditions (15 mM Mg²⁺, 0 or 10 μM SAM) that we considered most suitable for capturing the key states on the basis of the FRET histogram data (**Supplementary Fig. 1**). Of note, the high Mg²⁺ concentration was required to enhance the population of (high-FRET) AT states, so that a sufficient number of state interconversions can be sampled. The HMM analysis including FRET efficiency histogram validation, and the kinetic analysis of the HMM data are summarized in **Methods** and **Supplementary Fig. 3**.

HMM analysis on RS_{EA} in Mg²⁺ buffer in the absence of SAM ligands yielded a model with four states, depicted in different colors in the smFRET trace in **Fig. 3a**. The states are represented by disks (in corresponding colors) in the (average) FRET efficiency, $\langle E \rangle$, versus lifetime, τ , scatter plot in **Fig. 3b**. The analysis reveals a structurally compact (high-FRET) pair of states with short lifetimes, which we have already assigned to AT conformations above, and a structurally extended (low-FRET) pair of states (T conformations) with long lifetimes. Furthermore, the probabilities of state interconversion (**Fig. 3c**)^{38,39} indicate that the dynamics is dominated by fast (millisecond) switching between AT₁ and AT₂. Transitions between the T conformations and between T and AT conformations are much less frequent and occur on timescales greater than seconds. Apparently, high free energy barriers and, presumably, major secondary structure rearrangements are involved in these transitions.

The presence of SAM in the buffer changes the dynamics markedly, as is already obvious from the smFRET efficiency time traces (**Fig. 3d**). Also for these data, HMM analysis revealed a set of four interconverting states (**Fig. 3e**). The two (high-FRET) AT conformations have similar lifetimes as in the absence of SAM; the two (low-FRET) T conformations, however, have much shorter lifetimes than without SAM. Transitions between AT₁^{SAM} and AT₂^{SAM} are fast, as in the absence of SAM. All other transitions are significantly accelerated upon SAM binding and appear on timescales of a few ten to a hundred milliseconds (**Fig. 3f**), except for those between the AT₂^{SAM} and T₂^{SAM} states. Thus, SAM

binding not only affects the fractional populations (relative free energies) of the observed states, but markedly changes the barriers separating them from one another in the conformational free energy landscape.

Quantitative FRET histogram analysis

Having established the presence of four discrete FRET states in the RS_{EA} construct by HMM, we used this knowledge to disentangle the FRET histograms at all Mg^{2+} concentrations by globally fitting the entire data set with four Gaussian model distributions, introducing constraints on the peak positions at 15 mM Mg^{2+} to force consistency (within the error) to the HMM-determined values. The peak areas (fractional populations) and positions (average FRET efficiencies) of the distributions were allowed to vary with Mg^{2+} concentration according to a binding isotherm, $X([Mg^{2+}]) = X(0) + \Delta X / (1 + [Mg^{2+}]_{0.5} / [Mg^{2+}])$, with $[Mg^{2+}]_{0.5}$ representing the transition midpoint concentration. These fits describe all histograms very well (**Fig. 4a, Supplementary Fig. 1**) and reveal Mg^{2+} -dependent variations of the populations and average FRET efficiencies (**Fig. 4b, Supplementary Fig. 4a**), with $[Mg^{2+}]_{0.5}$ in the millimolar range.

The set of four FRET states should also apply to the other FRET-labeled construct, RS_{AA} , with identical (within the error) fractional populations and their variation with Mg^{2+} concentration, as long as dye labeling does not markedly affect the free energy differences. Peak positions in the FRET histograms, however, should generally differ due to the altered labeling positions. It may also happen that two states distinguishable in one FRET construct overlap and thus collapse into a single state in a differently labeled construct. In fact, this is the case for RS_{AA} because three Gaussians suffice to fit the entire set of smFRET histograms measured in the Mg^{2+} concentration range 0 – 100 mM (**Fig. 4c, Supplementary Fig. 2**). The well separated (cyan) distribution at $\langle E \rangle \approx 0.1$ shows an almost constant fractional population (**Fig. 4c**), matching the sum of the T_2 and AT_2 subpopulations identified for RS_{EA} (**Fig. 4a,b**), implying that these two states are not resolved in RS_{AA} . Accordingly, we globally fitted the FRET histograms, constraining the two predominant distributions T_1 (green) and AT_1 (red) to the same

fractional populations (within the error) as for RS_{EA} ; the resulting fit parameters are plotted in **Figure 4d** and **Supplementary Figure 4b**.

Thus, we have achieved a consistent description of the Mg^{2+} concentration dependence of the FRET histograms of both FRET-labeled constructs in the absence of SAM ligands. All FRET states determined from the experimental data are listed in **Supplementary Table 2**, including their peak positions $\langle E \rangle$ in buffer with low (<0.1 mM Mg^{2+}) and high (>20 mM Mg^{2+}) ionic strengths. In the presence of SAM, four additional states representing SAM-bound conformations would be required to fit the FRET efficiency histograms in the SAM titration experiments, which is entirely unfeasible. Therefore, we have restricted ourselves to modeling only the FRET efficiency histogram at a SAM concentration of 10 μ M, using the four states identified by HMM analysis (**Supplementary Fig. 1b** and **Supplementary Table 1**).

Structural and dynamic properties of SAM-I conformations

From the fractional state populations, we have calculated the relative free energies of the identified SAM-I riboswitch states at low and high Mg^{2+} concentrations and with SAM bound (**Fig. 5a–c**). Moreover, based on the kinetic network data (**Fig. 3c,f**), we used kinetic cluster analysis to compute the time scales of equilibration between states, τ_{eq} (see **Methods**)³⁸. These depend logarithmically on the free energy barriers that have to be surmounted during conformational transitions and are included in **Fig. 5b,c**. In addition, structural properties of the four states can be inferred from the observed average FRET efficiencies $\langle E \rangle$, yielding inter-dye distances R . Precise, quantitative comparison with structural models is not possible, however, because only (average) x-ray structures of the folded aptamer domain with and without bound ligand (at high ionic strength) are presently available^{17,24}, and the expression platform and joining regions can only be included by using simplified models. Nevertheless, we can gain some structural insights from FRET efficiency values and their comparison between states, as we will show below.

In the absence of SAM and Mg^{2+} ions, the smFRET histograms of RS_{AA} and RS_{EA} resemble one another (**Fig. 4a,b**). Both constructs have their acceptor on U_8 in the P1 region (**Fig. 1**) but the donor on different sites. Thus, the similar FRET histograms suggest that the two states present in both constructs differ structurally in the P1 region, featuring an open (lower FRET) and a compact, helical (higher FRET) P1 region for states T_2 and T_1 , respectively. Increasing the Mg^{2+} concentration stabilizes T_1 with respect to T_2 (**Fig. 5a,b**), and also causes a pronounced upshift of the T_1 FRET distribution, indicating a compaction of this conformation in both constructs (**Fig. 4a,b, Supplementary Fig. 4**). For T_1 of RS_{AA} , $\langle E \rangle = 0.61$ ($R = 49 \text{ \AA}$) at high Mg^{2+} concentration, which is in the expected range for two dye molecules attached via flexible linkers to a compact aptamer domain (**Fig. 5d**). For T_1 of RS_{EA} , $\langle E \rangle = 0.4$ ($R = 57 \text{ \AA}$) at high Mg^{2+} concentration, implying a compact arrangement of the expression platform moiety adjacent to the aptamer domain (**Fig. 5e**) rather than an extended structure. The slow equilibration between the two T states ($\tau_{eq} = 1.6 \text{ s}$) likely reflects the low probability of forming the P1 helix from nonadjacent strand segments.

The observation that the T_2 and AT_2 subpopulations are not resolved in the RS_{AA} construct (**Fig. 4c,d**) implies that the 5'-end of the P1 helix region is structured similarly in both states. Because strand invasion by the expression platform moiety in conformation AT_2 precludes formation of a complete P1 helix, this finding in turn supports our claim that a complete P1 helix is also absent in T_2 . We note, however, that an alternative base pairing may be possible in the P1 region even if the AT helix is formed, denoted by $P1'$ and $P1''$ in **Supplementary Figure 5**. Presumably, the putative $P1''$ helical region consisting of four base pairs is disrupted in AT_2 and the AT helix is stacked onto a partial P1 helix – a conformation proposed for the transcriptional ON state based on molecular modeling of a complete SAM riboswitch²⁷. The other AT conformation, AT_1 , has a higher $\langle E \rangle$ value than AT_2 , implying a smaller inter-dye distance R . AT_1 and AT_2 equilibrate very quickly ($\tau_{eq} = 0.03 \text{ s}$), suggesting that only small secondary structure rearrangements are involved. Accordingly, for AT_1 , a fold with a three-way junction consisting of the putative $P1'$ and $P1''$ stems and the AT helix would be compatible with these results. The slowest exchange is observed between the T_1/T_2 and AT_1/AT_2

state clusters ($\tau_{\text{eq}} = 3$ s) because this transition involves major secondary structure changes in the P1 helical region as well as in the expression platform.

In the SAM-bound riboswitch, we expect overall similar T state structures as without SAM. Their free energy difference is reduced (**Fig. 5c**), however, and their higher $\langle E \rangle$ values (**Supplementary Table 1**) may arise from better stabilized aptamer structure accompanied by SAM-induced P1 helix reorientation^{17,20} caused by direct contact formation between the ligand and nucleotides in the putative P1' helix region¹⁸ (U₁₄-A₁₁₉ and C₁₅-G₁₁₈ base pairs in our constructs). SAM binding has a pronounced effect on the AT conformations, raising their free energies relative to T₁ and T₂ (**Fig. 5b,c**). This behavior likely reflects the substantial stabilization of the P1 helix by the bound ligand in the T conformations.

Remarkably, the time for equilibration between the AT₁^{SAM}, AT₂^{SAM} and T₁^{SAM} states ($\tau_{\text{eq}} = 0.04$ s) is comparable to the one between the AT states without bound SAM ligand (**Fig. 5b,c**). Moreover, equilibration between T₂^{SAM} and the cluster of the other three states is substantially faster ($\tau_{\text{eq}} = 0.17$ s) than any transition involving ligand-free T states. The SAM-induced facilitated exchange between T and AT structures that we have observed here is likely associated with strand migration, in which AT helix base pairs convert to P1 helix base pairs and vice versa. There is indeed ample evidence for such a scenario, both from experiment and simulations^{27,40,41}. Notably, a 3 μ s unconstrained MD simulation showed such a strand migration event from an AT helix to a fully extended P1 helix⁴¹.

Discussion

Recent years have seen growing awareness that RNA molecules can fold into multiple, functionally relevant conformational states even in thermal equilibrium^{11,42}. The notion of a hierarchical energy landscape, originally introduced by Frauenfelder and collaborators to explain protein dynamics^{43,44}, has recently been adopted also for RNA dynamics^{10,13}. In this first smFRET study of the complete SAM-I riboswitch, we have identified four discrete states that are significantly populated in thermal equilibrium over wide ranges of Mg^{2+} and SAM ligand concentrations. Comparison of the free energy landscapes governing SAM-I riboswitch dynamics with and without a SAM ligand reveals only gradual changes, with the two AT states shifting to higher energies upon SAM binding (**Fig. 5b,c**). Interestingly, T_1 is the most stable state, regardless of whether SAM is bound or not. Thus, our results support the notion that gene regulation by the SAM-I riboswitch is “not like flipping a switch but more like tuning a dimmer”⁴⁵. Qualitatively similar, limited population changes upon ligand binding have earlier been reported for the FMN riboswitch¹⁴.

The conformational energy landscape of the SAM-I riboswitch is strongly affected by Mg^{2+} counter ions. SAM ligands form additional tertiary interactions that stabilize the aptamer domain upon binding, specifically the P1 helix nucleation region. In a recent smFRET study on the much smaller preQ₁ riboswitch, Walter and coworkers⁴⁶ revealed mechanistic details as to how the energy landscape is sculpted by Mg^{2+} and the ligand, which are in line with our results on SAM-I riboswitch conformational dynamics (**Fig. 5**). At low Mg^{2+} concentration, we found an overall open, highly fluctuating riboswitch structure. SAM will then bind to and thereby stabilize those riboswitch folds that can engage in hydrogen bonds to the bound SAM (induced-fit mechanism). At high Mg^{2+} concentration, the riboswitch structure is compact and well stabilized by Mg^{2+} ions. Multiple secondary folds of T and AT conformations co-exist, and the SAM ligand preferably associates with those conformations resembling the bound state, i.e., with stacked P4 and P1 helices (conformational selection).

At millimolar ion concentrations in the absence of SAM, T conformations are predominant in equilibrium, although AT conformations are also present in measurable quantities (**Fig. 4b,d**), and interconversions between T and AT occur with characteristic times of a few seconds or more (**Fig. 5e**). Because transcriptional riboswitches sense the presence of the ligand cotranscriptionally, the dynamics of conformational change may be important for the biological function of the riboswitch^{12,14,28}, and not merely equilibrium properties. There is a brief window of opportunity during which the ligand can bind to the nascent riboswitch before the RNA polymerase has reached the start site of the downstream gene, controlled by the processivity of RNA polymerase ($\sim 40\text{--}90\text{ nt/s}^{47}$) and possibly pausing sites. It has been argued that the SAM-I riboswitch preferentially folds into the AT conformation because AT helix formation from proximal nucleotides is faster than P1 helix formation from distal base pairs^{27,48,49}. Moreover, the first Watson-Crick base pair stabilizing the T hairpin (U₁₅₃–A₁₅₇) can form only after incorporation of A₁₅₈ (**Fig. 1a,b**). At this point in time, however, the AT hairpin region extending from A₁₂₁ to U₁₅₆ is already completed, which also supports the notion that folding of the SAM-I riboswitch into the AT conformation upon mRNA elongation is favorable. We have shown that interconversion between AT and T states is slow without SAM bound to the aptamer domain (**Fig. 5b**). Consequently, the unliganded riboswitch will persist in the AT conformation, i.e., in the transcriptional ON state for typically several seconds. If SAM binds at an early stage, however, it stabilizes the P1 nucleation site and increases the probability for the expression platform to fold into the T conformation. Even if the AT hairpin forms initially, the dramatic acceleration of transitions between T and AT conformations (**Fig. 5c**) ensures that the riboswitch can swiftly change to the thermodynamically more stable T conformation, i.e., the transcriptional OFF state. Indeed, the accelerated dynamics upon SAM binding appears to be crucial for the proper biological function of the SAM-I riboswitch.

Acknowledgments

The authors thank Alexander Schug (KIT) for fruitful discussions. This work was supported by a grant from the Karlsruhe Heidelberg Research Partnership (HEiKA, to A.J. and G.U.N.). A.J. acknowledges additional funding by the Volkswagen Foundation and the Deutsche Forschungsgemeinschaft (DFG) through grant CRC 1114. G.U.N. was also supported by the Helmholtz program Science and Technology of Nanosystems (STN), Karlsruhe School of Optics and Photonics (KSOP), and DFG grant GRK 2039.

Author contributions

G.U.N. and A.J. designed research, A.S. synthesized RNA constructs, C.M. and A.Y.K. built the experimental setup and took data, C.M., A.Y.K. and B.G.K. analyzed data, and all authors contributed to manuscript writing.

Competing financial interests

The authors declare no competing financial interest.

Additional information

Supplementary information is available in the online version of the paper.

Methods

Synthesis of riboswitch constructs. Chemicals were purchased from Sigma-Aldrich unless otherwise stated. Dye-labeled RNA oligonucleotides and the splint DNA were obtained from IBA. The non-labeled RNA oligonucleotides bearing a 5'-phosphate were purchased from Dharmacon (GE Healthcare). The riboswitch was synthesized by splinted ligation from four 34-mer and one 33-mer RNA sequences: 5'-AUA UCC GUU CUU AUC AAG AGA AGC AGA GGG ACU G-3', 5'-GCC CGA CGA UGC UUC AGC AAC CAG UGU AAU GGC G-3', 5'-AUC AGC CAU GAC UAA GGU GCU AAA UCC AGC AAG C-3', 5'-UCG AAC AGC UUG GAA GAU AAG AAG AGA CAA AAU C-3' and 5'-ACU GAC AAA GUC UUC UUC UUA AGA GGA CUU UUU-biotin-3'. RNA fragments were FRET dye-labeled by selective substitution of the underlined uridines, depending on the desired riboswitch construct, with 5-[3-[(6-aminohexyl)amino]-3-oxo-1-propenyl]-uridine and post-synthetic derivatization of the primary amino groups using NHS-esters of Cy3 and Cy5. FRET pair-labeled riboswitch constructs were synthesized on the 3-nmol scale.

During all incubations of dye-labeled oligonucleotides, the samples were protected from ambient light by wrapping them in aluminum foil. During preparative gel purification of ligated constructs, the gels were covered with aluminum foil. All preparative gels contained a separate analytical lane. During scanning of the gels on the Typhoon 9400 imager (GE Healthcare), only this analytical lane was exposed for scanning; the preparative lane was covered with aluminum foil to protect it from the Typhoon laser. The band position in the preparative lane was marked by taking guidance from the band position in the analytical lane. The preparative band was excised under minimal light.

Enzymatic 5'-phosphorylation of RNA fragments (40 μ M final concentration) was performed with T4 polynucleotide kinase (Fermentas, 0.75 U/ μ l final concentration) in kinase buffer (50mM Tris-HCl, pH 7.4, 10mM MgCl₂, 2mM ATP and 5mM DTT) at 37°C for 60 min while shaking at 600 rpm, followed by phenol-ether extraction and ammonium acetate (pH 5.6, 0.5 M final concentration)

precipitation. The RNA pellets were vacuum-dried and dissolved in water. For the formation of the ligation-competent complex, the five RNA fragments (10 μ M each; all fragments were phosphorylated except for the one at the 5'-end of the riboswitch) were annealed to the complementary full-length DNA splint (9.5 μ M) by heating to 90 °C for 1 min, followed by cooling for 15 min to room temperature in ligation buffer (50 mM Tris-HCl, pH 7.4, 10 mM MgCl₂, 50 μ M ATP, 5 mM DTT). Subsequently, T4 RNA ligase 2 (0.5 μ M, NEB) was added and the mixture was incubated at 37 °C while shaking at 600 rpm for 1 h. For digesting the DNA splint, DNase I (Fermentas, 0.5 U/ μ l final concentration) was added and the resulting mixture was incubated at 37 °C while shaking for 15 min at 600 rpm. The reaction was stopped by adding gel loading buffer (90% formamide, 1 \times Tris-borate-EDTA buffer), heating for 15 s to 90 °C followed by snap-cooling in ice and submitted to denaturing PAGE (8% gel). Bands corresponding to the full-length riboswitch were excised from the gel and eluted using 0.5 M ammonium acetate (pH 5.6) solution by overnight shaking at 20 °C, followed by ethanol precipitation. After drying, the RNA pellet was re-dissolved in water and the RNA concentration was determined using a NanoDrop ND-1000 spectrophotometer (Peachlab). This optimized 5-piece ligation protocol yielded ~10% of full-length RNA, as determined by comparing the fluorescence intensity of the desired band to that of the total fluorescence intensity of the analytical lane on the gel (Typhoon 9400 imager).

Sample preparation. Experiments were carried out with smFRET samples kept in home-made microfluidic chambers constructed from two glass coverslips (24 \times 32 mm² and 20 \times 20 mm²). After removing contaminants by flaming over a Bunsen burner, the coverslips were glued together by using double-sided adhesive tape, leaving a 2 mm wide channel in the middle. The channel was thoroughly rinsed with distilled water and then flushed with a 1 mg/ml solution of biotinylated bovine serum albumin (BSA) in phosphate buffered saline (PBS, pH 7.4) to prevent unspecific adsorption of RNA on the glass surface^{32,50}. To prepare samples of properly folded, surface immobilized RNA molecules, the chambers were incubated with a streptavidin solution (10 μ g/ml, in PBS) prior to adding the sample solution containing FRET labeled SAM-I riboswitch molecules.

Aliquots of the SAM-I riboswitch stock solution were diluted to a concentration of 10–100 pM in standard riboswitch buffer (50 mM Tris-HCl, pH 7.4, 100 mM NaCl) with 15 mM MgCl₂ added, followed by heating to 70 °C for 2 min and slow cooling to room temperature. Subsequently, the solution was pipetted into the microfluidic chamber. Unbound RNA molecules were removed by extensive flushing of the chamber with standard riboswitch buffer, supplemented with MgCl₂ and SAM ligands so as to achieve the desired concentrations. Dye photobleaching was minimized by adding oxygen scavenging⁵¹ and triplet quenching systems⁵² (1 μM protocatechuate 3,4-dioxygenase (PCD), 2 mM protocatechuic acid (PCA), 1 mM Trolox, 1 mM cyclooctatetraene (COT), 1 mM nitrobenzyl alcohol (NBA), and 1 mM 2-mercaptoethylamine (MEA)) to the sample solution immediately before the measurement was started.

Single-molecule FRET microscopy. Experiments on freely diffusing or immobilized RS_{EA} molecules were performed by using a home-built confocal microscope based on a Zeiss Axiovert 35 frame (**Supplementary Fig. 6**)^{32,53}, which was modified as follows: FRET marker dyes Cy3 (donor) and Cy5 (acceptor) were excited by a 532 nm laser (Excelsior 532, Nd-YAG laser, Spectra Physics) and a 637 nm laser (Obis 637, Coherent), respectively. Both laser beams were coupled into a single-mode fiber (QSMJ-3AF3S, OZ Optics) to create clean and spatially uniform beam profiles. A programmable beam splitter depicted schematically in **Supplementary Figure 7** was employed to achieve high detection efficiency in multi-color excitation and multi-channel detection experiments.⁵⁴ To obtain precisely overlapping foci, all four laser beams were laterally and axially aligned by using a pair of dispersion compensating prisms (prism 1 and prism 2) and two sets of adjustable mirrors ($M_2 - M_5$, $M_2^* - M_5^*$, **Supplementary Fig. 6**). To ensure that data were only recorded on RNA molecules labeled with a functional FRET pair of dyes, we employed an alternating laser excitation (ALEX) scheme⁵⁵ by continually switching the excitation between donor (70 μs) and acceptor (30 μs) with a 5 μs blank interval in the detection during color-switching to exclude temporal cross-talk. The fluorescence emission was collected by a water immersion objective (UPlan Apo 60x /1.2w, Olympus), passed through either a 100 μm (for freely diffusing molecules) or 50 μm (for immobilized molecules)

pinhole, and separated by dichroic mirror DM2 (640DCXR, Chroma) into the donor (green) and acceptor (red) detection channels (**Supplementary Fig. 6**). The light was passed through filters (BrightLine HC 580/60 and HC 642/LP for the green and red channels, respectively; Semrock), and single photons were detected by avalanche photodiodes (APD, SPCM-AQR-14, Perkin Elmer Optoelectronics). Counts were registered by a data acquisition card (PCI 6602, National Instruments) synchronized with the excitation cycle. Samples were positioned by using a XY piezoelectric stage (P-731.20, Physik Instrumente) with analog voltage control by a multi-functional data acquisition card (PCI 6229, National Instruments). For the experiments on freely diffusing molecules, the sample was continuously moved along a circle with 30 μm diameter at 25 $\mu\text{m s}^{-1}$ to avoid optically biased diffusion effects⁵⁶. We acquired data on immobilized molecules by moving the piezo stage across a field of 30 \times 30 μm^2 to collect images of 128 \times 128 pixels with 5 ms pixel dwell time. A program written in C++ permitted real-time control of all electronic devices and completely automated data acquisition.

Experiments on immobilized RS_{AA} molecules were performed on a home-built prism-type total internal reflection fluorescence (pTIRF) microscope based on a Zeiss Axiovert 200 frame (**Supplementary Fig. 8**)⁵⁷. Cy3 and Cy5 FRET-labeled RNA molecules were excited by 532 nm (DPGL-2050F, SUWTech) and 638 nm (MLD 638, Cobolt AB) lasers, respectively. The laser beams were individually aligned by a set of mirrors, passed through an AOTF (AA Opto-electronic) for fast power modulation, expanded by a pair of apochromatic lenses (L1: focal length 30 mm, L2: focal length 100 mm, both ThorLabs) to achieve homogeneous illumination over a wide field of view, and focused slightly behind the sample coverslip by the apochromatic lens L3 with a focal length of 300 mm (ThorLabs). The excitation light was coupled into the quartz glass specimen holder (Finkenbeiner) by using a Pellin-Broca quartz prism (Eksma Optics) for maximum efficiency and minimal scattering. The excitation power was controlled by reflecting 5% of the light onto a power meter (Artifex Engineering). The fluorescence emission was collected with a water immersion objective (C-Apochromat 63 \times /1.2w, Zeiss), separated from the excitation light by a dichroic filter (HQ550LP,

Chroma) and a notch filter (NF03-633E-25, Semrock), then spatially filtered by a rectangular slit, and split into two spectral channels by a dichroic mirror (650DCXRU, Chroma). The images of the two colors were projected side by side onto an EMCCD camera (iXon EM+ DU-897, Andor Technology).

FRET histogram analysis on freely diffusing molecules. SAM-I riboswitch molecules (50pM) were dissolved in buffer (50mM Tris, 100mM NaCl, pH 7.4) supplemented with the desired concentration of Mg^{2+} ions and SAM ligands. To obtain good statistics, we collected several thousand photon fluorescence bursts from single molecules diffusing through the focus to calculate FRET efficiency values by ratiometric analysis of donor and acceptor intensities. We included only events with 0.2 – 2 ms duration and total photon counts (in both donor and acceptor channels upon 532 nm excitation) of more than 50. The donor (I_D^{Gr} , $I_D^{Rd} \approx 0$) and acceptor (I_A^{Gr} , I_A^{Rd}) intensities obtained with green and red excitation, respectively, were corrected for the ensemble-averaged background and spectral cross-talk. FRET efficiency values were calculated from individual bursts according to

$$E = \frac{I_A^{Gr}}{I_A^{Gr} + \gamma I_D^{Gr}} \quad (1)$$

and compiled into FRET histograms^{31,58}. Here, γ represents the dye-specific detection efficiency parameter.

FRET histogram analysis on immobilized molecules. Riboswitch molecules were attached to BSA-covered glass slides via biotin-streptavidin linkage^{32,50}. The slides were imaged with the pTIRFM system using 1s camera dwell time. Using a freely available smFRET data acquisition and analysis software package (<https://cplc.illinois.edu/software>), single molecules were identified, and their emission intensities in the two color channels were integrated and background-corrected. To obtain good statistics, several thousand individual molecules were registered, and their FRET efficiency was calculated by using equation 1, with γ determined by means of a stoichiometry map⁵⁵.

Fast kinetics and HMM analysis. From a large number of smFRET donor and acceptor intensity time traces of immobilized RS_{EA} molecules, we selected those data sets for HMM analysis that showed anti-correlated donor and acceptor intensity fluctuations and single-step photobleaching after an extended period of time. A strict validation procedure finally resulted in eight optimal intensity time traces each for RS_{EA} molecules in Mg^{2+} buffer with and without SAM, corresponding to overall measurement durations of 246 and 108 s, respectively. Accordingly, a few hundred transitions were observed between states interconverting on the time scale of 100 ms. For each trace, background, cross-talk of the donor signal into the acceptor detection channel and the γ factor were extracted. Details of the HMM analysis including optimization and validation procedures have been described elsewhere³⁸. Briefly, the HMM workflow consists of the following steps: (i) for a chosen number of hidden states, 100 models with random parameters are constructed and optimized by using the expectation-maximization algorithm for a few iterations only; (ii) afterwards, the model with the largest likelihood is optimized to full convergence. (iii) Steps (i) and (ii) are repeated multiple (here 20) times to confirm reproducibility of the obtained model. Specifically, the heuristic criterion for reproducibility is that the model with the highest log-likelihood should be identified in at least 20% of all trials. In this procedure, two models are considered identical if their log-likelihood differs by less than 1.0. (iv) The solution is validated by testing its Markovianity; i.e., residence times within each state estimated from the maximum-likelihood path must follow an exponential distribution. Results of the Markovianity test are shown in **Supplementary Figure 3**. (v) From the maximum-likelihood path, FRET photon time traces of the donor and acceptor dyes are generated by randomly drawing from Poisson distributions. The rate parameter of the Poisson distributions is time-dependent and calculated from the hidden state at every time point t and the overall photon count rate. From these synthetic photon emission traces, FRET histograms with different binning times (e.g., 10, 50 and 250 ms) are estimated to test for consistency with the experimental data. (vi) The previous steps are repeated by increasing the number of states until a reproducible, validated Markov model is obtained. The rationale behind this approach is that, for systems with molecular

dynamics governed by a hierarchical energy landscape, the model describes the data better if fast-interconverting states (e.g., states differing by the conformation of a highly dynamic loop) are represented by separate hidden states rather than by a single state corresponding to the average of the fast-interconverting subensemble. For the interpretation of the model, these states can be regrouped into a single subensemble by kinetic clustering methods (see below)⁵⁹. In this study, HMM analysis revealed four-state models for SAM-I riboswitches in buffer with and without SAM ligands.

Kinetic state clustering. Characteristic time scales of transitions between states are calculated from an eigenvalue/eigenvector analysis of the transition matrix **T** containing all microscopic rate coefficients (**Fig. 3c,f**)⁵⁹. Each eigenvalue λ_i of the transition matrix **T**, except for $\lambda_1 = 1$ describing the stationary process, is associated with transitions between individual states or state clusters described by the associated eigenfunctions. The characteristic time scale of equilibration within the clusters of states is defined as

$$\tau_{eq_i}(\Delta t) = -\frac{\Delta t}{\ln(\lambda_i)}, \quad (2)$$

where Δt is the time resolution of the experimental data. As a result of interconversions, the multi-dimensional conformational energy landscape may degenerate to a one-dimensional dominant pathway on longer observational time scales, for which cluster analysis identifies the hierarchy and timescale of transitions⁵⁹.

Data availability. The data that support the findings of this study are available from the corresponding author upon reasonable request.

Code availability. Software packages custom-developed for HMM analysis and eigenvalue/eigenvector analysis of the HMM transition matrix are available from Bettina Keller (bettina.keller@fu-berlin.de) upon request.

References

1. Montange, R.K. & Batey, R.T. Structure of the S-adenosylmethionine riboswitch regulatory mRNA element. *Nature* **441**, 1172-1175 (2006).
2. Winkler, W.C., Nahvi, A., Sudarsan, N., Barrick, J.E. & Breaker, R.R. An mRNA structure that controls gene expression by binding S-adenosylmethionine. *Nat. Struct. Biol.* **10**, 701-707 (2003).
3. Winkler, W.C. & Breaker, R.R. Genetic control by metabolite-binding riboswitches. *ChemBioChem* **4**, 1024-1032 (2003).
4. Montange, R.K. & Batey, R.T. Riboswitches: emerging themes in RNA structure and function. *Annu. Rev. Biophys.* **37**, 117-133 (2008).
5. Breaker, R.R. Prospects for riboswitch discovery and analysis. *Mol. Cell* **43**, 867-879 (2011).
6. Tucker, B.J. & Breaker, R.R. Riboswitches as versatile gene control elements. *Curr. Opin. Struct. Biol.* **15**, 342-348 (2005).
7. Wang, J.X. & Breaker, R.R. Riboswitches that sense S-adenosylmethionine and S-adenosylhomocysteine. *Biochem. Cell Biol.* **86**, 157-168 (2008).
8. Trausch, J.J. et al. Structural basis for diversity in the SAM clan of riboswitches. *Proc. Natl. Acad. Sci. USA* **111**, 6624-6629 (2014).
9. McDaniel, B.A., Grundy, F.J., Artsimovitch, I. & Henkin, T.M. Transcription termination control of the S box system: direct measurement of S-adenosylmethionine by the leader RNA. *Proc. Natl. Acad. Sci. USA* **100**, 3083-3088 (2003).
10. Mustoe, A.M., Brooks, C.L. & Al-Hashimi, H.M. Hierarchy of RNA functional dynamics. *Annu. Rev. Biochem.* **83**, 441-466 (2014).
11. Furtig, B., Nozinovic, S., Reining, A. & Schwalbe, H. Multiple conformational states of riboswitches fine-tune gene regulation. *Curr. Opin. Struct. Biol.* **30**, 112-124 (2015).
12. Lemay, J.F., Penedo, J.C., Tremblay, R., Lilley, D.M. & Lafontaine, D.A. Folding of the adenine riboswitch. *Chem. Biol.* **13**, 857-868 (2006).
13. Greenleaf, W.J., Frieda, K.L., Foster, D.A., Woodside, M.T. & Block, S.M. Direct observation of hierarchical folding in single riboswitch aptamers. *Science* **319**, 630-633 (2008).
14. Wickiser, J.K., Winkler, W.C., Breaker, R.R. & Crothers, D.M. The speed of RNA transcription and metabolite binding kinetics operate an FMN riboswitch. *Mol. Cell* **18**, 49-60 (2005).
15. Neupane, K., Yu, H., Foster, D.A., Wang, F. & Woodside, M.T. Single-molecule force spectroscopy of the add adenine riboswitch relates folding to regulatory mechanism. *Nucl. Acids Res.* **39**, 7677-7687 (2011).
16. Rieder, U., Kreutz, C. & Micura, R. Folding of a transcriptionally acting preQ1 riboswitch. *Proc. Natl. Acad. Sci. USA* **107**, 10804-10809 (2010).
17. Stoddard, C.D. et al. Free state conformational sampling of the SAM-I riboswitch aptamer domain. *Structure* **18**, 787-797 (2010).
18. Montange, R.K. et al. Discrimination between closely related cellular metabolites by the SAM-I riboswitch. *J. Mol. Biol.* **396**, 761-772 (2010).
19. Heppell, B. & Lafontaine, D.A. Folding of the SAM aptamer is determined by the formation of a K-turn-dependent pseudoknot. *Biochemistry* **47**, 1490-1499 (2008).
20. Heppell, B. et al. Molecular insights into the ligand-controlled organization of the SAM-I riboswitch. *Nat. Chem. Biol.* **7**, 384-392 (2011).
21. Klein, D.J., Schmeing, T.M., Moore, P.B. & Steitz, T.A. The kink-turn: a new RNA secondary structure motif. *EMBO J.* **20**, 4214-4221 (2001).
22. Winkler, W.C., Grundy, F.J., Murphy, B.A. & Henkin, T.M. The GA motif: an RNA element common to bacterial antitermination systems, rRNA, and eukaryotic RNAs. *RNA* **7**, 1165-1172 (2001).
23. McDaniel, B.A., Grundy, F.J. & Henkin, T.M. A tertiary structural element in S box leader RNAs is required for S-adenosylmethionine-directed transcription termination. *Mol. Microbiol.* **57**, 1008-1021 (2005).

24. Lu, C. et al. SAM recognition and conformational switching mechanism in the Bacillus subtilis yitJ S box/SAM-I riboswitch. *J. Mol. Biol.* **404**, 803-818 (2010).
25. Aboul-ela, F., Huang, W., Elrahman, M.A., Boyapati, V. & Li, P. Linking aptamer-ligand binding and expression platform folding in riboswitches: prospects for mechanistic modeling and design. *WIREs RNA* **6**, 631-650 (2015).
26. Hennelly, S.P., Novikova, I.V. & Sanbonmatsu, K.Y. The expression platform and the aptamer: cooperativity between Mg²⁺ and ligand in the SAM-I riboswitch. *Nucl. Acids Res.* **41**, 1922-1935 (2013).
27. Boyapati, V.K., Huang, W., Spedale, J. & Aboul-Ela, F. Basis for ligand discrimination between ON and OFF state riboswitch conformations: the case of the SAM-I riboswitch. *RNA* **18**, 1230-1243 (2012).
28. Frieda, K.L. & Block, S.M. Direct observation of cotranscriptional folding in an adenine riboswitch. *Science* **338**, 397-400 (2012).
29. Kurschat, W.C., Müller, J., Wombacher, R. & Helm, M. Optimizing splinted ligation of highly structured small RNAs. *RNA* **11**, 1909-1914 (2005).
30. Chung, H.S. & Gopich, I.V. Fast single-molecule FRET spectroscopy: Theory and experiment. *Phys. Chem. Chem. Phys.* **16**, 18644-18657 (2014).
31. Dammertz, K., Hengesbach, M., Helm, M., Nienhaus, G.U. & Kobitski, A.Y. Single-molecule FRET Studies of counterion effects on the free energy landscape of human mitochondrial lysine tRNA. *Biochemistry* **50**, 3107-3115 (2011).
32. Kobitski, A.Y., Nierth, A., Helm, M., Jäschke, A. & Nienhaus, G.U. Mg²⁺-dependent folding of a Diels-Alderase ribozyme probed by single-molecule FRET analysis. *Nucl. Acids Res.* **35**, 2047-2059 (2007).
33. Rieger, R., Kobitski, A., Sielaff, H. & Nienhaus, G.U. Evidence of a folding intermediate in RNase H from single-molecule FRET experiments. *ChemPhysChem* **12**, 627-633 (2011).
34. Hennelly, S.P. & Sanbonmatsu, K.Y. Tertiary contacts control switching of the SAM-I riboswitch. *Nucl. Acids Res.* **39**, 2416-2431 (2011).
35. Pirchi, M. et al. Single-molecule fluorescence spectroscopy maps the folding landscape of a large protein. *Nat. Commun.* **2**, 493 (2011).
36. McKinney, S.A., Joo, C. & Ha, T. Analysis of single-molecule FRET trajectories using hidden Markov modeling. *Biophys. J.* **91**, 1941-1951 (2006).
37. Lee, T. Extracting kinetics information from single-molecule fluorescence resonance energy transfer data using hidden Markov models. *J. Phys. Chem. B* **113**, 11535-11542 (2009).
38. Keller, B.G., Kobitski, A., Jäschke, A., Nienhaus, G.U. & Noé, F. Complex RNA folding kinetics revealed by single-molecule FRET and hidden Markov models. *J. Am. Chem. Soc.* **136**, 4534-4543 (2014).
39. Prinz, J.H. et al. Markov models of molecular kinetics: generation and validation. *J. Chem. Phys.* **134**, 174105 (2011).
40. Huang, W., Kim, J., Jha, S. & Aboul-ela, F. Conformational heterogeneity of the SAM-I riboswitch transcriptional ON state: a chaperone-like role for S-adenosyl methionine. *J. Mol. Biol.* **418**, 331-349 (2012).
41. Huang, W., Kim, J., Jha, S. & Aboul-ela, F. The impact of a ligand binding on strand migration in the SAM-I riboswitch. *PLoS Comput. Biol.* **9**, e1003069 (2013).
42. Reining, A. et al. Three-state mechanism couples ligand and temperature sensing in riboswitches. *Nature* **499**, 355-359 (2013).
43. Frauenfelder, H., Sligar, S.G. & Wolynes, P.G. The energy landscapes and motions of proteins. *Science* **254**, 1598-1603 (1991).
44. Nienhaus, G.U., Müller, J.D., McMahon, B.H. & Frauenfelder, H. Exploring the conformational energy landscape of proteins. *Physica D* **107**, 297-311 (1997).
45. Baird, N.J., Kulshina, N. & Ferre-D'Amare, A.R. Riboswitch function flipping the switch or tuning the dimmer? *RNA Biol.* **7**, 328-332 (2010).

46. Suddala, K.C., Wang, J., Hou, Q. & Walter, N.G. Mg²⁺ shifts ligand-mediated folding of a riboswitch from induced-fit to conformational selection. *J. Am. Chem. Soc.* **137**, 14075-14083 (2015).
47. Vogel, U. & Jensen, K.F. The RNA chain elongation rate in Escherichia coli depends on the growth rate. *J. Bacteriol.* **176**, 2807-2813 (1994).
48. Huang, W., Kim, J., Jha, S. & Aboul-ela, F. A mechanism for S-adenosyl methionine assisted formation of a riboswitch conformation: a small molecule with a strong arm. *Nucl. Acids Res.* **37**, 6528-6539 (2009).
49. Whitford, P.C. et al. Nonlocal helix formation is key to understanding S-adenosylmethionine-1 riboswitch function. *Biophys. J.* **96**, L7-L9 (2009).
50. Heyes, C.D., Kobitski, A.Y., Amirgoulova, E.V. & Nienhaus, G.U. Biocompatible surfaces for specific tethering of individual protein molecules. *J. Phys. Chem. B* **108**, 13387-13394 (2004).
51. Aitken, C.E., Marshall, R.A. & Puglisi, J.D. An oxygen scavenging system for improvement of dye stability in single-molecule fluorescence experiments. *Biophys. J.* **94**, 1826-1835 (2008).
52. Dave, R., Terry, D.S., Munro, J.B. & Blanchard, S.C. Mitigating unwanted photophysical processes for improved single-molecule fluorescence imaging. *Biophys. J.* **96**, 2371-2381 (2009).
53. Kuzmenkina, E.V., Heyes, C.D. & Nienhaus, G.U. Single-molecule Förster resonance energy transfer study of protein dynamics under denaturing conditions. *Proc. Natl. Acad. Sci. USA* **102**, 15471-15476 (2005).
54. Seyfried, V., Birk, H., Storz, R. & Ulrich, H. Advances in multispectral confocal imaging. *Proc. SPIE* **5139**, 147-157 (2003).
55. Kapanidis, A.N. et al. Fluorescence-aided molecule sorting: analysis of structure and interactions by alternating-laser excitation of single molecules. *Proc. Natl. Acad. Sci. USA* **101**, 8936-8941 (2004).
56. Osborne, M.A., Balasubramanian, S., Furey, W.S. & Klenerman, D. Optically biased diffusion of single molecules studied by confocal fluorescence microscopy. *J. Phys. Chem. B* **102**, 3160-3167 (1998).
57. Sacca, B. et al. Reversible reconfiguration of DNA origami nanochambers monitored by single-molecule FRET. *Angew. Chem. Int. Ed.* **54**, 3592-3597 (2015).
58. Kobitski, A.Y., Hengesbach, M., Helm, M. & Nienhaus, G.U. Sculpting an RNA conformational energy landscape by a methyl group modification – a single-molecule FRET study. *Angew. Chem. Int. Ed.* **47**, 4326-4330 (2008).
59. Noé, F., Horenko, I., Schutte, C. & Smith, J.C. Hierarchical analysis of conformational dynamics in biomolecules: transition networks of metastable states. *J. Chem. Phys.* **126**, 155102 (2007).

Figure Captions

Figure 1. Structural depictions of the SAM-I riboswitch. Secondary structure models of the *B. subtilis* *ytJ* SAM-I riboswitch (169-nt fragment) in the **(a)** terminator (T) and **(b)** anti-terminator (AT) conformations. Helices P1 (orange), P2 (magenta), P3 (blue) and P4 (green) form the aptamer; the expression platform is colored in dark red. Base pairing of the T structure and the AT stem-loop is depicted by lines according to McDaniel et al.²³. Donor (Cy3) and acceptor (Cy5) dye labeling sites of the two labeled constructs (RS_{AA} and RS_{EA}) are shown as green and red stars, respectively. Biotin is represented by a black diamond at the 3'-end. **(c)** Schematic of the tertiary structure of the T conformation. The aptamer domain is overlaid on a crystal structure of the SAM-I riboswitch (PDB ID 4KQY)²⁴ shown in the background. Helices P1-P4 and T are depicted as cylinders in the same colors as in panels (a, b). PK and KT denote the pseudoknot and kink-turn motifs of the P2 helix, respectively; the SAM binding site is marked by an arrow. Green and red stars indicate the donor and acceptor fluorophores, respectively. **(d)** Schematic of the tertiary structure of the AT conformation. Helices P2, P3 and P4 are shown as in the crystal structure of the aptamer domain. The AT and partial P1 helices are depicted in a stacked conformation as proposed earlier²⁷.

Figure 2. Mg^{2+} - and ligand-dependent folding of SAM-I riboswitch. Histograms of smFRET efficiency values of riboswitch constructs exposed to different buffer solutions: **(a)** RS_{AA} at 0, 7.5 and 25 mM Mg^{2+} , **(b)** RS_{EA} at 0, 6.25 and 25 mM Mg^{2+} , **(c)** RS_{EA} at 0, 10 and 100 nM SAM in the presence of 20 mM Mg^{2+} . Schematic depictions of structural changes revealed by the FRET histograms: **(d)** Mg^{2+} -induced folding of the aptamer domain that causes the shift of the main peak, **(e)** Mg^{2+} -induced transition from the T to the AT structure, and **(f)** SAM-induced transition from the AT to the T conformation.

Figure 3. HMM analysis of conformational dynamics of the SAM-I riboswitch. **(a)** Typical smFRET efficiency time trace measured on immobilized RS_{EA} molecules exposed to buffer conditions with 15 mM Mg^{2+} . Data were averaged in 100 ms time bins or less for shorter intervals. **(b)** Two-dimensional scatter plot of four states identified by HMM, represented by disks with areas proportional to their

equilibrium populations, as a function of FRET efficiency and lifetime. **(c)** Kinetic network of state interconversion, with microscopic rate coefficients given in the unit [s^{-1}] next to the corresponding arrows. For rare transitions on the order of $10^{-2} s^{-1}$, these numbers represent only upper bounds because of insufficient sampling. Different widths of the arrows represent fluxes (equilibrium population times rate coefficient) of order (thick) 10^{-3} , (intermediate) 10^{-4} and (thin) $10^{-5} s^{-1}$. **(d-f)** Data corresponding to those in panels (a-c) for RS_{EA} molecules in buffer containing 15 mM Mg^{2+} and 10 μ M SAM.

Figure 4. Global fit analysis of smFRET efficiency histograms. **(a, b)** Fit of the RS_{EA} smFRET data with a four-state model: T_1 (green), T_2 (blue), AT_1 (red), AT_2 (orange). **(c, d)** Fit of the RS_{AA} smFRET data with the three-state model: T_1 (green), AT_1 (red), and $T_2 + AT_2$ (cyan) states. **(a,c)** Histograms at selected Mg^{2+} concentrations are plotted together with the best-fit Gaussian distributions of individual states (colored lines) and their sums (dashed lines), and **(b,d)** fractional populations obtained from the global fit. Error bars represent uncertainties given by the non-linear least-squares fitting software (OriginPro 2015). Dashed lines in (d) depict the fractional populations for the RS_{EA} construct as in (c); the cyan line gives the sum of the blue and orange dashed lines.

Figure 5. SAM-I riboswitch conformational states and their properties. **(a-c)** Free energies at (a) 0 mM Mg^{2+} , (b) 15 mM Mg^{2+} and (c) 15 mM Mg^{2+} and 10 μ M SAM, calculated from ratios of state populations, P_i , by using $\Delta G_{AB} = -RT \ln(P_A/P_B)$, with R and T denoting the gas constant and absolute temperature, respectively. The free energies of states T_1 and T^{SAM} were set to zero in the plots. **(b,c, top)** Equilibration times between states along the transition pathway, plotted on a logarithmic axis. **(d-f)** Schematic depictions of conformational states and transitions. (d) At low Mg^{2+} concentration, two T states with an expanded aptamer domain coexist. (e) High Mg^{2+} concentration causes a compaction of the aptamer domain, and two AT states are also present in equilibrium. (f) At high Mg^{2+} concentration, the aptamer is further stabilized by SAM ligand binding; two pairs of T and AT states are again observed in equilibrium.

Figures

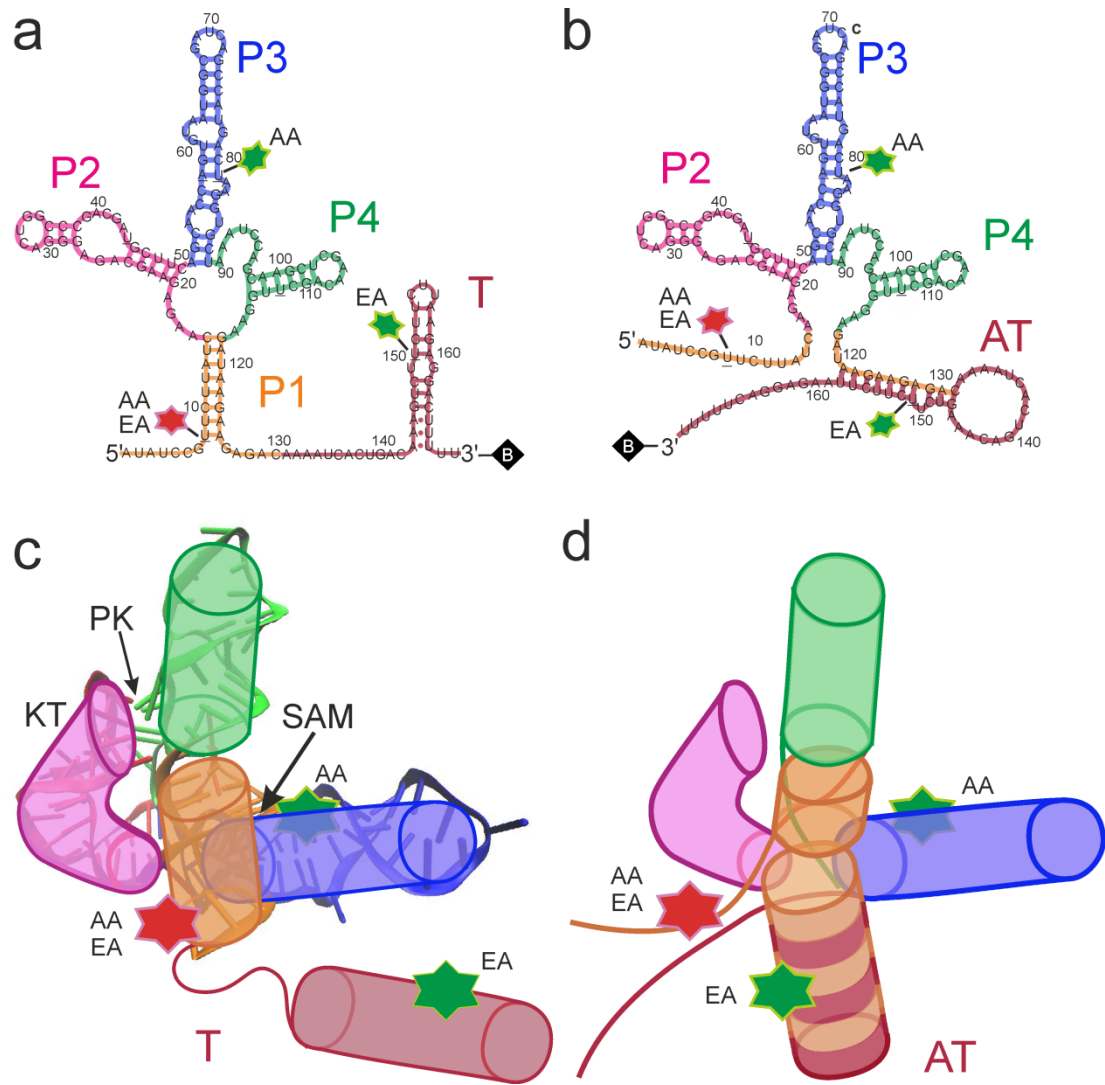


Figure 1

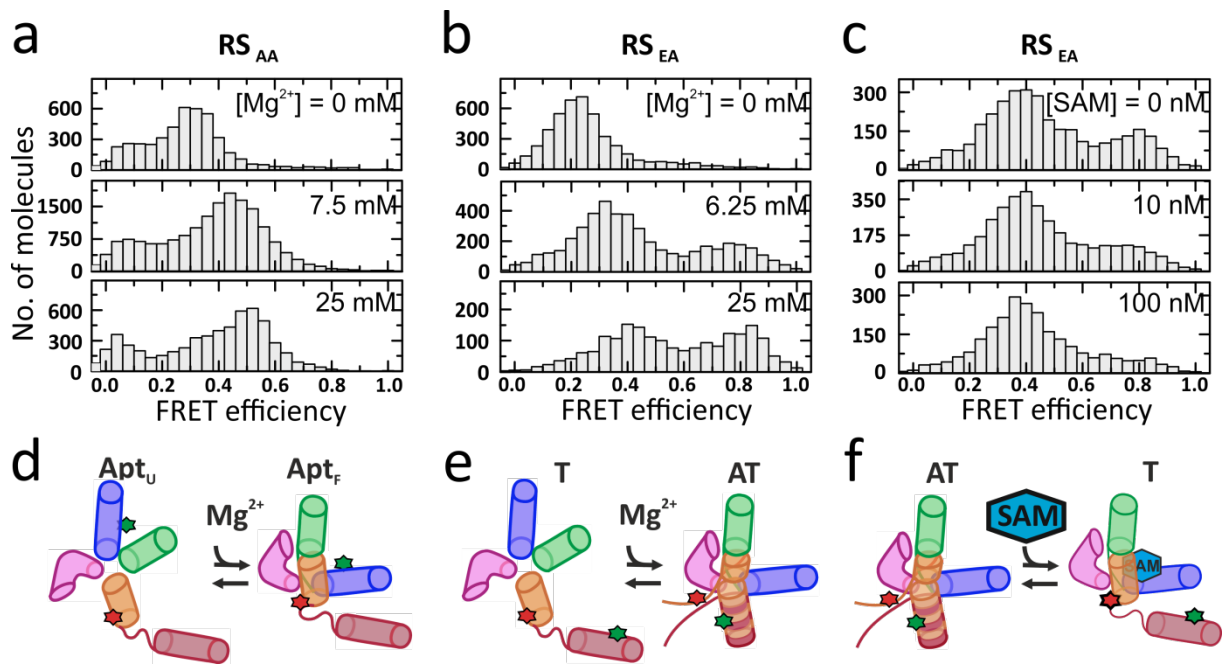


Figure 2

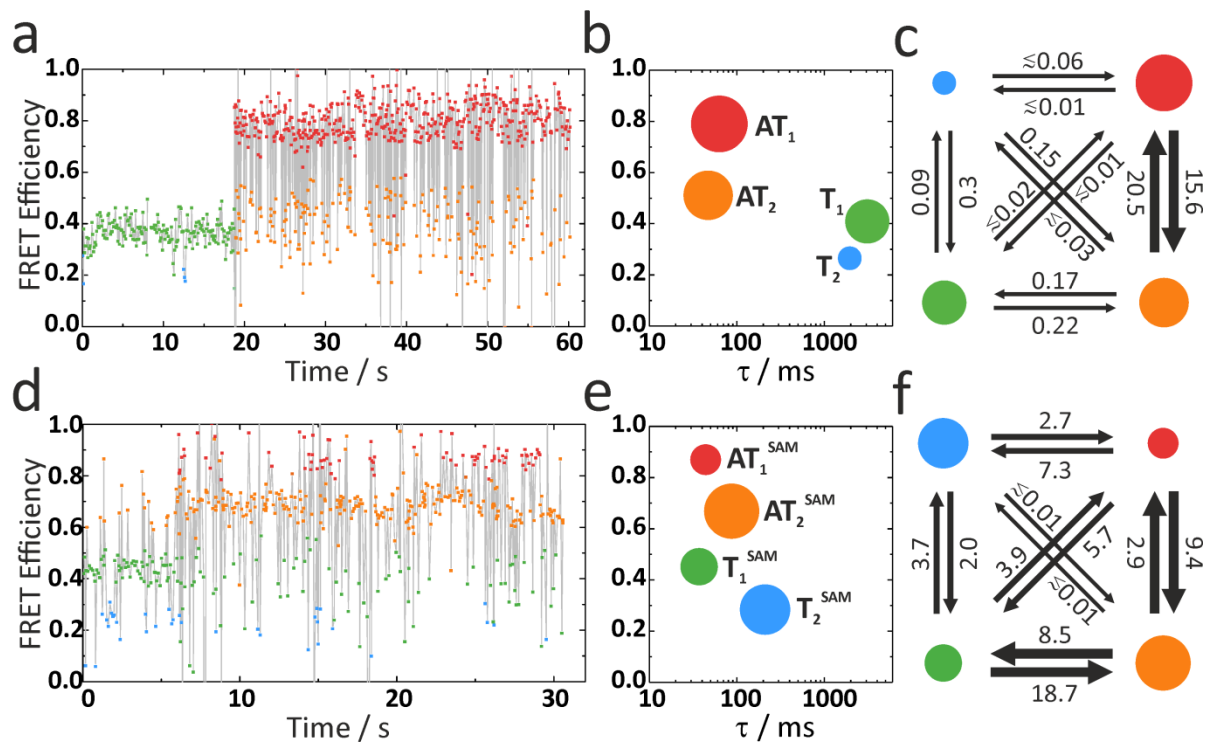


Figure 3

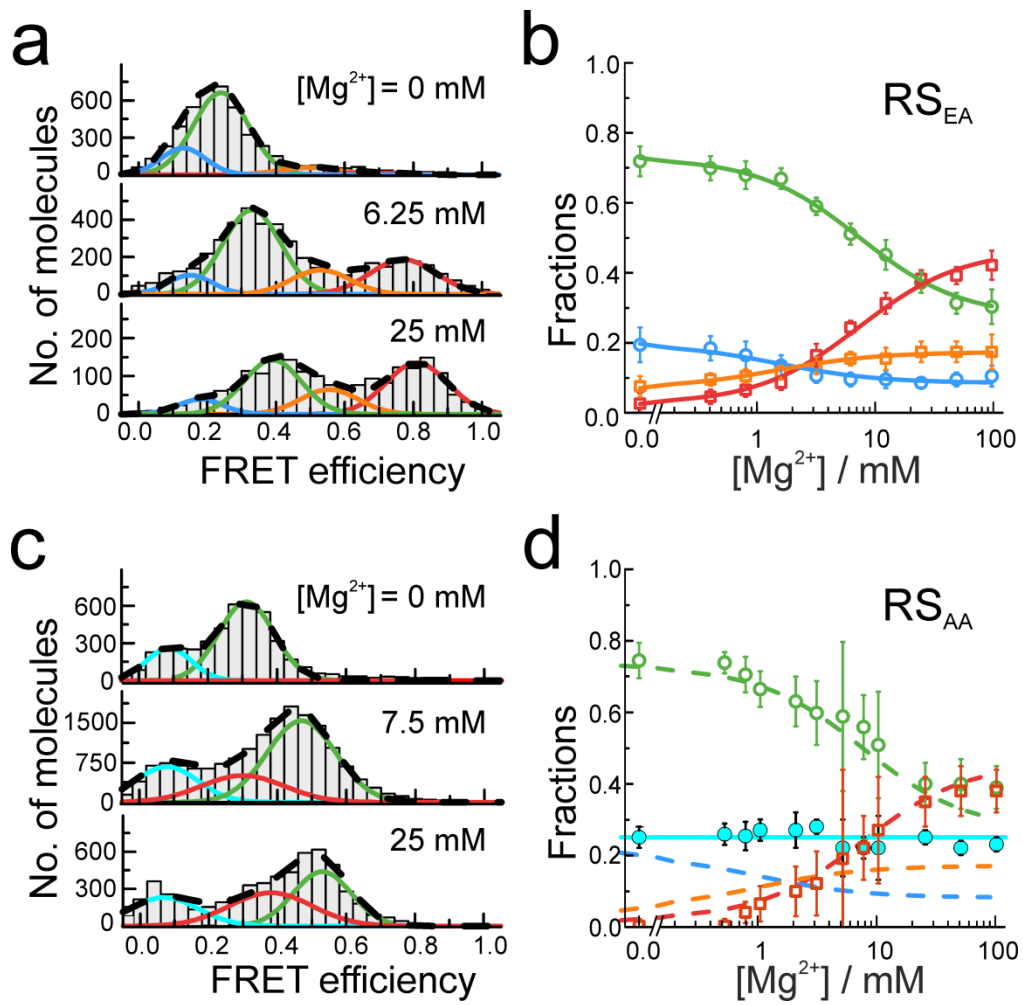


Figure 4

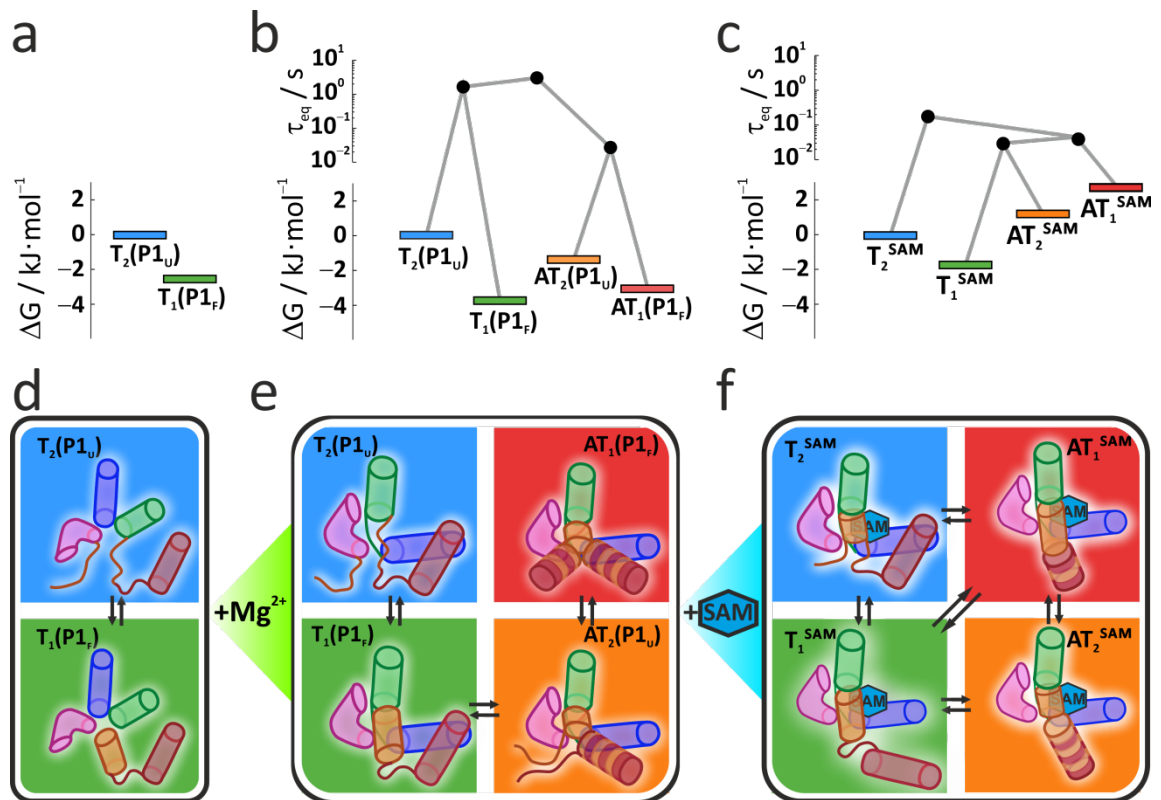


Figure 5